*Scandinavian Journal of Metallurgy 2004; **33:** 98–104*
Printed in Denmark. All rights reserved

SCANDINAVIAN JOURNAL OF METALLURGY

A numerical study of an insulating end-quench test for high hardenability steels

Xin Yao[1], Jianfeng Gu[1], Mingjuan Hu[1] and Zuchang Zhu[2]

[1]*College of Materials Science & Engineering, Shanghai Jiao Tong University, Shanghai;* [2]*Department of Materials Science & Engineering, Shanghai Polytechnic University, Shanghai, China*

A numerical model is presented to determine the heat transfer, phase transformation and hardness distribution of extension Jominy bars in an insulating end-quenching test designed to evaluate the hardenablility of steels having middle or high hardenability. The end-quenching test is conducted in a revised device with a refractory insulating liner to decrease the cooling rate of the specimen. Heat transfer coefficients varying not only with temperature of end surface but also with radius are adopted when examining the water jet on the end side. A modified model based on Avrami equation and Koistien–Marburger law is developed to determine the microstructure distribution, and an empirical based formula developed by Maynier is applied to calculate the Vickers hardness of each phase at different cooling rate. The microstructure and hardness predictions obtained in the present model are found to be in good agreement with experimental measurements.

Key words: end-quenching test, hardenability, numerical simulation.

Accepted for publication 30 June 2003

A large amount works have been done on the Jominy test since 1938 when it was first devised by Jominy and Boegehold [1–3]. Recently, some researchers [4, 5] have developed models to simulate the Jominy test numerically, mostly concentrated on hardness and hardenability prediction. Li [6], for example, presented a finite element model to simulate the heat transfer induced by end quenching of Jominy bars, and a reaction kinetics model for austenite decomposition. The calculated hardness distributions of the bars based on the empirical formulas are in good agreement with the experimental measurements for all the tested steels. In another work, Andersson [7] investigated the hardness values of a cylindrical specimen made of direct quenching steels based on the Jominy curves, and also gave good results.

The standard Jominy end-quench test, however, is not suitable for the steels with high hardenability, because the Jominy curves cannot exhibit the hardness variation of these steels in the full measurement range. Post [8] and Jatczak [9] presented air-cooling devices that are suitable for high hardenability steel. But because air and water are different cooling medium with quite different heat transfer mechanisms, the end-quench results obtained by air-cooling methods and standard Jominy test cannot be comparative.

In the present work, an insulating Jominy end-quench test is developed to determine the hardenability of AISI P20 and ASSAB718 plastic mold steel. This revised Jominy test greatly decreases the cooling rate of the cylinder top, and therefore, can obtain wider range of cooling rate in the full length of the specimen. In the meantime, a mathematical model is presented and implemented to describe the temperature, structure and hardness variations of the process, and the calculation results are then compared with the experimental ones.

Model description

Heat transfer model

A two-dimensional axisymmetric finite element model is developed to analyze the heat transfer induced by the revised end-quenching process using the commercial code MSC.MARC and user-defined subroutines. The finite element mesh of the bar is presented in Fig. 1.

During cooling by a water jet on the end surface, the top and most of the cylindrical surfaces of the bar are in contact with the refractory insulating material, and a small portion of the cylindrical surface is subjected to free convection in air and radiation. Therefore, the boundary conditions of the problem should be

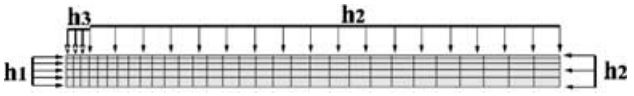

Fig. 1. Finite element mesh of the end-quenching bar and thermal boundary conditions.

$$-\sum_k V_k\lambda_k(T)\frac{\partial T}{\partial z} = \begin{cases} h_1(T_s - T_w) & \text{End surface} \\ h_2(T_s - T_r) & \text{Top surface} \end{cases}$$

$$-\sum_k V_k\lambda_k(T)\frac{\partial T}{\partial r} = \begin{cases} h_3(T_s - T_a) & \text{From } z = 0 \text{ to } z = L_0 \text{ of the lateral surface} \\ h_2(T_s - T_r) & \text{From } z = L_0 \text{ to the top of the lateral surface} \end{cases}$$

$$\frac{\partial T}{\partial r} = 0 \quad \text{on the axis} \tag{1}$$

wherein T_s, T_w, T_a and T_r stand for the temperatures of the sample surface, jetting water, surrounding air, and refractory insulating material contacted, respectively. V_k and λ_k are the volume fraction and heat conductivity of kth phase. L_0 represents the portion of the specimen outside the insulating sleeve. Different cooling methods are represented by different heat transfer coefficients, e.g., h_1 is the convection heat transfer coefficient of water jetting, h_2 is the combined convective and radiation heat transfer coefficient of air cooling and h_3 is used to express the heat transfer from the specimen to the refractory insulating material, as shown in Fig. 1. We have attempted here to take into account a heat transfer coefficient of end surface h_1 varying not only with temperature of end surface but also with the radius [10]. When examining the water jet on the end side, the heat transfer coefficient of a point arresting in the center (in $r = 0$) is first determined according to Fig. 2. Heat transfer coefficient on the end surface depending on the radius r is estimated as

$$h(r) = -5 \times 10^5 r^5 + 0.0017r^4 - 0.0187r^3 + 0.0571r^2 + 0.1367r + 0.4076. \tag{2}$$

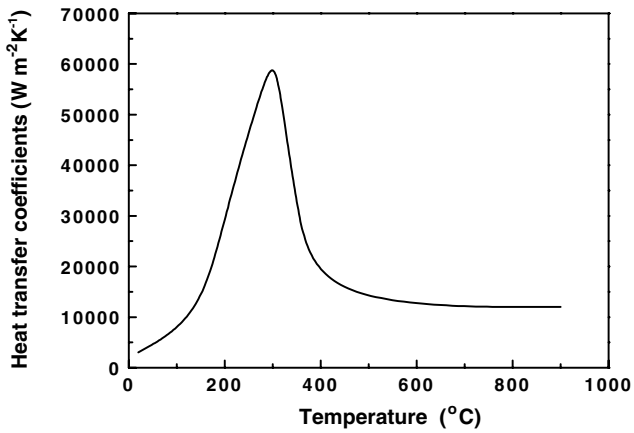

Fig. 2. Hypothesis for the heat transfer coefficients on the quenching end.

Heat loss through free surfaces is also incorporated into the analysis by introducing the combined heat transfer of convection and radiation. The heat loss through the insulating material is far less than through water and air, and therefore, it is neglected in the present model and assuming $h_3 = 0$.

For latent heats we also take the values from [11, 12]

$$L_{F/P} = 1.56 \times 10^9 - 1.5 \times 10^6 \text{T(J/m}^3\text{)}, L_B = 6.2 \times 10^8 \text{(J/m}^3\text{)}, L_M = 8.4 \times 10^8 \text{(J/m}^3\text{)}. \tag{3}$$

Phase transformation model

The reaction kinetics model developed in this study is based on the modification of the original model developed by Pan [13]. The Scheil additivity rule is adopted to determine the time at which the phase transformation begins. At every Δt increment after the beginning of the phase transformation, John–Mehl–Avrami equation is used to determine the virtual time and quantities of the diffusional phases, and iteration with temperature is activated at the same time. In the case of martensitic transformation, between M_s and M_f temperatures, the amount of martensite is calculated by using the law established by Koistinen and Marburger. Moreover, the following specification should be mentioned in this paper.

1 The models presented by Pan [13] did not consider the irreversibility of the phase transformation. Thus, in numerical simulations based on these models, owing to the release of latent heat, usually a decrease in the transformed phase is observed. In the present model, in order to overcome the evident irrationality, the following rules are defined in the subroutines

$$V_k(i) = \begin{cases} V_k(i) & V_k(i) \geq V_k(i-1) \\ V_k(i-1) & V_k(i) \leq V_k(i-1) \end{cases} \quad k = \text{F, P, B, M} \tag{4}$$

where $V_k(i)$ is the volume fraction of kth phase in ith increments.

2 In the temperature region between A_{c1} and B_s, both ferrite and pearlite may precipitate. Because the nucleation locations, growth modes and diffusion paths of carbon atoms are different for the two phases, different Avrami equations should be adopted to calculate the phase growth. However, the beginning point of pearlite transformation is hard to determine during continuous cooling, in respect that the carbon content of austenite is continuously changing during transformation, and the transformed pearlite is quasi-pearlite and its carbon content is decreasing with the decrease of temperature. Actually, Avrami equation is a generalized one in describing the kinetics of diffusional transformations, and the parameters b and n in the equation include the

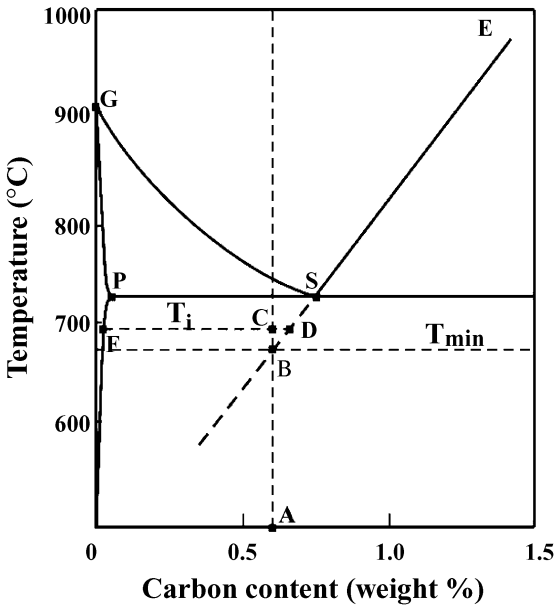

Fig. 3. Illustration of the iron–carbon diagram used in the calculation of ferrite and pearlite.

influence of various factors such as nucleation location and growth mode. It was also found that in this temperature region, the simulated transformation results using a single Avrami equation were more close to the experimental measurements [14].

An approximate method to determine the quantities of the two phases can be described in the Fe–C diagram as shown in Fig. 3, where line AB represents the equivalent carbon content of AISI P20 or ASSAB 718 steel, point S is the eutectoid point, and line SB is the quasi-eutectoid precipitation line. Suppose in an incremental step, with the temperature of T_i, the relative volume fraction of ferrite and pearlite can be determined using the level rule. Therefore, the maximal amount of ferrite ($V_{F\max}$) at that temperature is equal to CD/FD. After the total amount of ferrite and pearlite (V_{tot}) is calculated by eq. (5), the two phases are divided according to the following rule:

$$\begin{aligned}&\text{(i) if } V_{\text{tot}} \le V_{F\max}\text{, then } V_F = V_{\text{tot}},\ V_P = 0\\ &\text{(ii) if } V_{\text{tot}} \ge V_{F\max}\text{, then } V_F = V_{\text{tot}},\ V_P = V_{\text{tot}} - V_{F\max}\end{aligned} \quad (5)$$

where V_F and V_P are the amount of transformed ferrite and pearlite respectively. When the temperature is below $T_{\min}$ (referring to Fig. 3), only quasi-eutectoid pearlite precipitates.

Hardness prediction model

Hardness prediction is based on the results of temperature and microstructure calculation. Empirically based formulas developed by Maynier et al. [15] were used in this study for calculation of the Vickers hardness of each phase at different cooling rate:

$$\begin{aligned}Hv_M &= 127 + 949\text{C} + 27\text{Si} + 11\text{Mn} + 8\text{Ni} + 16\text{Cr} + 21 \times \log Vr\\ Hv_B &= -323 + 185\text{C} + 330\text{Si} + 153\text{Mn} + 65\text{Ni} + 144\text{Cr} + 191\text{Mo} + (89 + 53\text{C} - 55\text{Si} - 22\text{Mn} - 10\text{Ni} - 20\text{Cr} - 33\text{Mo}) \log Vr\\ Hv_{F+P} &= 42 + 223\text{C} + 53\text{Si} + 30\text{Mn} + 12.6\text{Ni} + 7\text{Cr} + 19\text{Mo} + (10 - 19\text{Si} + 4\text{Ni} + 8\text{Cr} + 130V) \log Vr\end{aligned} \quad (6)$$

where Hv_M, Hv_B *and* Hv_{F+P} represent the Vickers hardness of martensite, bainite and the mixture of ferrite and pearlite, respectively. Vr is the cooling rate at 700°C per hour.

The overall hardness of the bar is calculated using the mixture rule

$$Hv = \sum_k Hv_k \cdot V_k \quad k = \text{F, P, B, M.} \quad (7)$$

The resultant Vickers hardness was transformed into Rockwell hardness in the subroutines to correlation with the experimental measured results.

The insulating Jominy end-quench test

AISI P20 and ASSAB718, both used as plastic mold steel, were chosen as experimental materials. P20 steel has middle hardenability, while ASSAB718 steel, with 0.80–1.20 wt% more nickel in its composition, has much higher hardenablility. The compositions of these two steels are listed in Table 1. In order to determine the hardenability of the two mold steels, a device based on the standard Jominy end-quench tester is devised. The principle characteristic of this device is that a sleeve made of refractory insulating fiber, as shown in Fig. 4, insults the overall end-quenching process. Extension Jominy bars made of AISI P20 and ASSAB718 steel are cut for 200 mm in length and 25 mm in diameter, each with a step on the top side to facilitate fixation. After heating at 860°C for 30 min, the test bar is transferred promptly to the inner core of the sleeve, and cooled by a water jet on its end. The water temperature keeps around 20°C. A portion of the bar on the end side (about 10 mm) is outside the sleeve to prevent the insulating material from getting wet. The end-quenching process lasts for 2 h until the bar is cooled completely, and then it was taken out and polished parallel to the cylinder axis on both sides. Rockwell hardness measurements are made along the

Table 1. *Chemical composition of AISI P20 and ASSAB718 steel*

	C	Si	Mn	S	P	Cu	Cr	Ni	Mo
AISI P20	0.28	0.20	0.60	0.03	0.03	0.25	1.40	0.25	0.3
ASSAB718	0.32	0.20	1.00	0.03	0.03	0.31	1.40	0.80	–

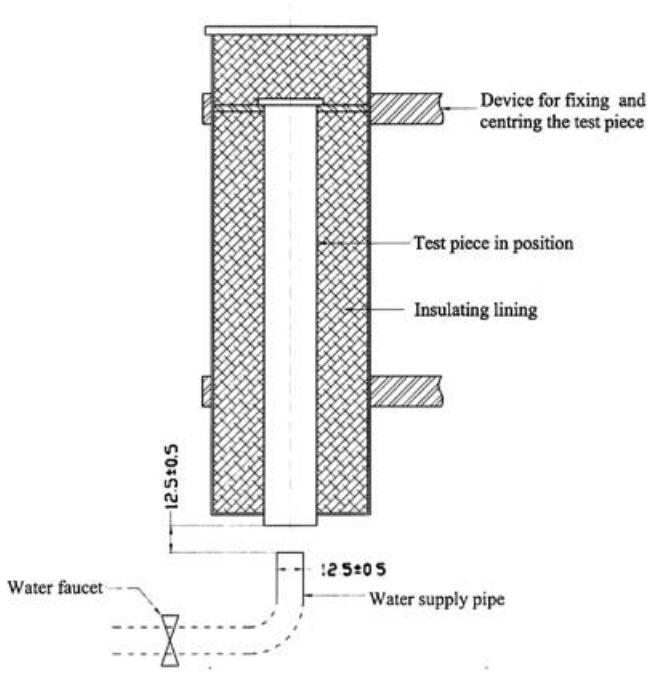

Fig. 4. The illustration of the insulating end-quenching device.

longitudinal axis from the quenching end, and metallographic examination is conducted to the regions with evident characteristics.

Results and discussion

Thermal cycles in the end-quenching bar

Finite element analysis revealed that the cooling curves in different bars are virtually the same despite of the minor differences in the thermal properties of the two steels. The predominant heat transfer mechanism in the end quench of the bars is forced convection at the quenching end. Heat is primarily carried away by the jetting water, and heat loss through free radiation and convection of cylindrical surfaces and through conduction of the insulating material is less significant.

The predicted cooling curves in the end-quenching bars are shown in Fig. 5. The bucklings of the cooling curves indicate the release of latent heat during phase transformations. In the present study, because the bar is longer than the standard Jominy bar and is encapsulated with insulating material, its cooling rate is slower than that of the standard Jominy bar. However, The results of experimental and finite element analysis and analytical solutions also suggest that the cooling curves in different standard Jominy bars are virtually identical despite the differences in steel composition, material properties and austenization temperatures [2]. As can be seen from the figure, a wide range of cooling rate can

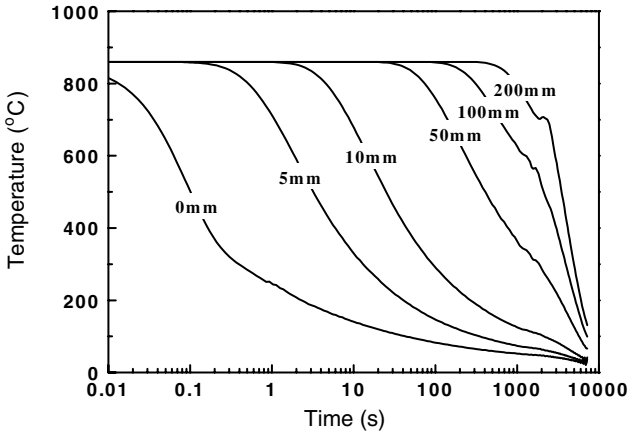

Fig. 5. Predicted cooling curves of the end-quenching bar.

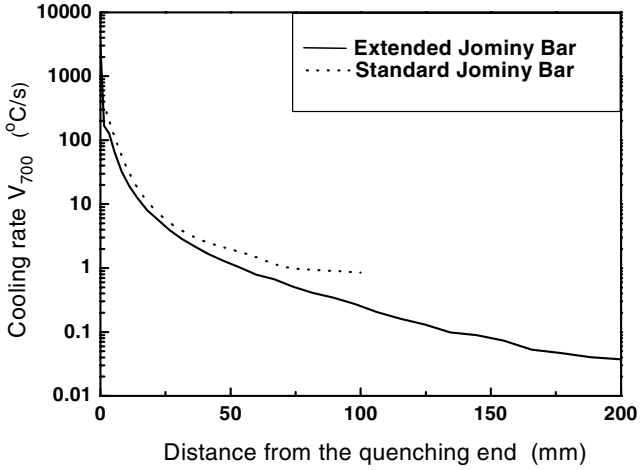

Fig. 6. Relationship between distance from water-cooled end to cool rate at 700°C.

be obtained by using this end-quenching method. For example, the time required for the bar to cool from the initial temperature of 860 to 200°C is 40 s at the point 5 mm away from the quenched end, while 6000 s is needed at the point 200 mm away from the quenching end.

The computed cooling rates at 700°C of the AISI P20 steel bar are shown in Fig. 6, associated with that of the standard bar determined by Herring [2]. For the above-mentioned reasons, the cooling rate of the present study is much slower than that of the standard Jominy test, especially in positions far away from the quenching end.

Microstructure results

The predicted and measured microstructure distribution along the AISI P20 steel bar after 7200 s of end quenching is presented in Figs. 7(a)–(e). As can been seen from Fig. 7(a), martensite extends in the region from the quenching end to a height of about 25 mm;

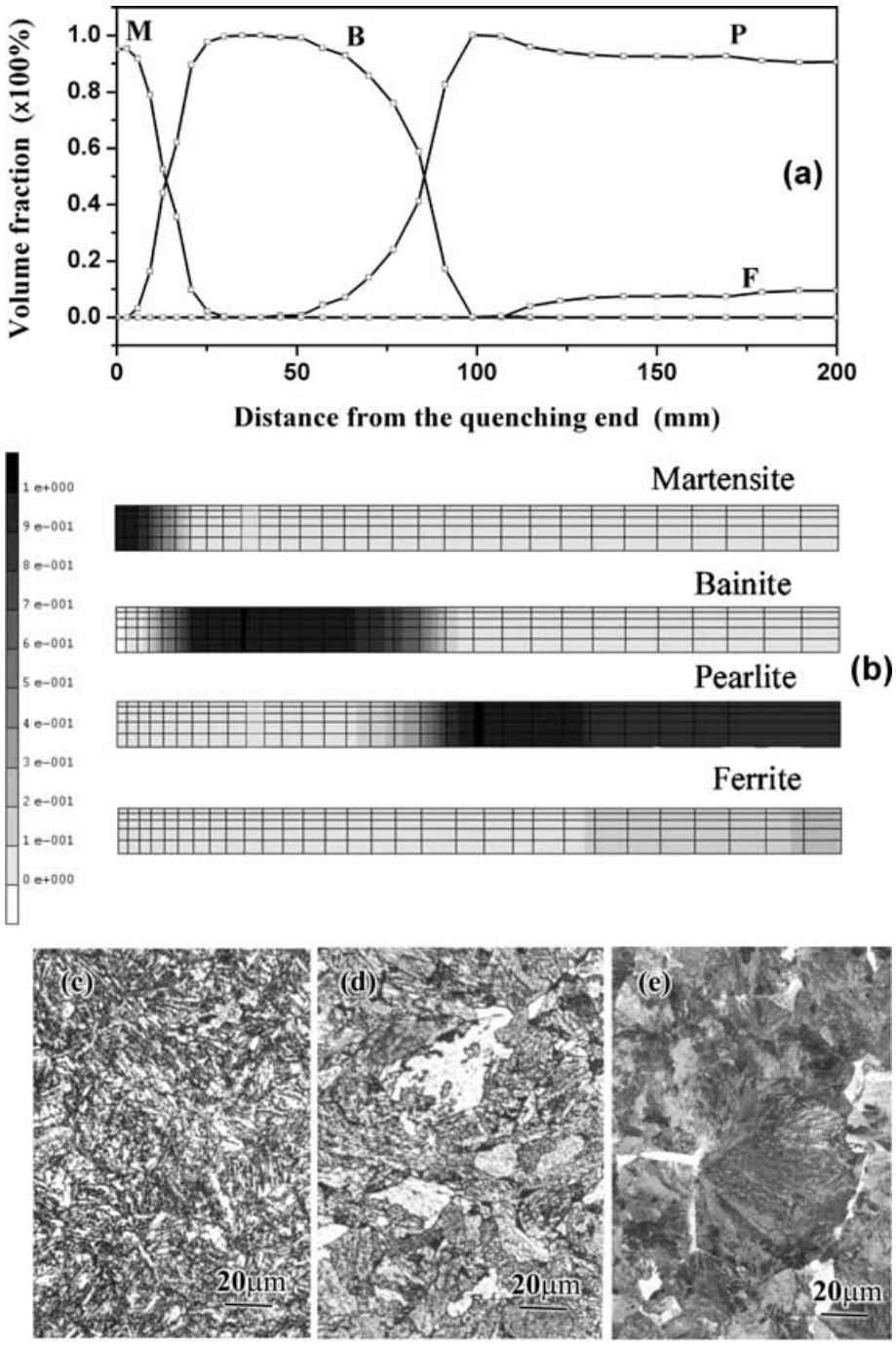

Fig. 7. Calculated and experimental results of structures distribution of AISI P20 steel after 7200 s of end-quenching: (a) calculated results of structures distribution; (b) contour of structure distribution; (c) metallograph of the quenching end (martensite); (d) metallurgraph of the section 50 mm from the quenching end (bainite) and (e) metallograph of the section 150 mm from the quenching end (pearlite).

bainite exists in the region between 10 mm and 110 mm; pearlite and a little fraction of ferrite lie in the region beyond 50 mm from the quenching end. In Fig. 7(b), the contour plot of martensite, bainite, pearlite and ferrite is presented. The metallographic analysis results are given in Figs. 7(c)–(e), and the specimens are taken from the quenching end, 45 mm and 150 mm away from the quenching end, respectively. The corresponding microstructures are lath and lamellar martensite, granular bainite and eutectoid structure with a little fraction of ferrite in the grain boundaries, respectively, which agree quite well with the calculated results.

Similar to AISI P20 steel, numerical and experimental analysis were also conducted on ASSAB718 steel and the results are shown in Figs. 8(a)–(d). Unlike AISI P20 steel, the austenite in ASSAB718 steel bar decomposes into only two phases, martensite and bainite

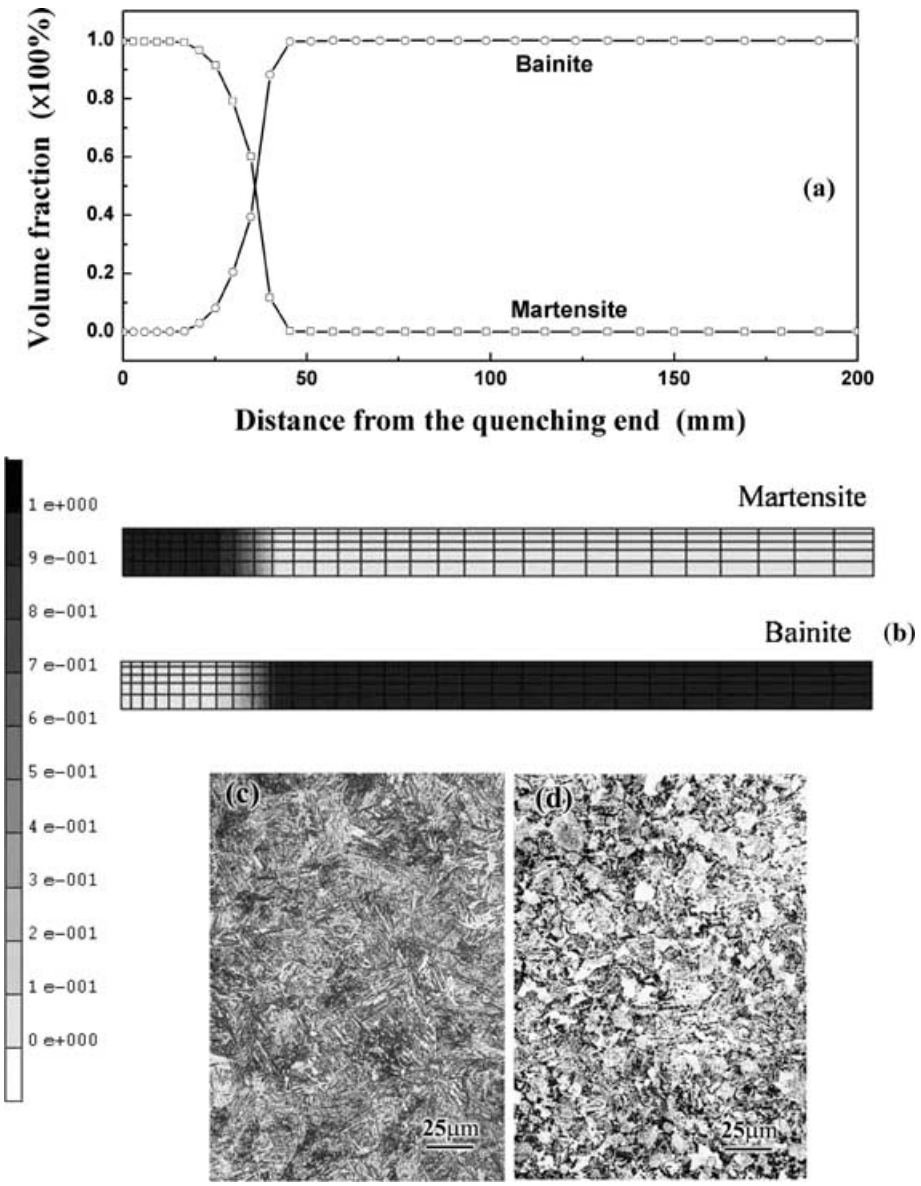

Fig. 8. Calculated and experimental results of microstructure distribution of ASSAB 718 steel after 7200 s of end-quenching: (a) calculated results of microstructure distribution; (b) contour of microstructure distribution; (c) metallograph of the quenching end (martensite); (d) metallograph of the section 150 mm from the quenching end (bainite).

after end quenching from the same austenizing temperature. The volume fractions of the two phases along the end-quenching bar are given in Fig. 8(a). The contour plots of the two phases after 7200 s of end quenching are also shown in Fig. 8(b). The region in which the volume fraction of martensite is in excess of 50 pct extends from the surface to a depth of about 37 mm, and the rest region is mostly consists of bainite. No pearlite and ferrite are found in the calculation of end quenching of ASSAB718 steel. The metallographic analysis results are given in Figs. 8(c) and (d). It can be seen from the figures that martensite is formed in the quenching end of ASSAB718 steel, and granular bainite is found in the region 150 mm away from the quenching end. It can be drawn from the above-mentioned figures that the predicted microstructure distributions are in good agreement with the experimentally measured results.

Hardness prediction

Though hardness is a principal investigation performance of the end-quenching test, the hardness predictions, because of the numerous factors (e.g. the cooling rate, microstructure, steel composition, etc.) that affect the hardness values, are quite difficult. Most of the present models of hardness predictions are based on empirical formulas, which are highly dependant on the experimental conditions, steel types, and so on.

According to the calculated microstructure results, along with the cooling rates of each node at 700°C (see Fig. 6), the hardness profiles of AISI P20 steel bar are

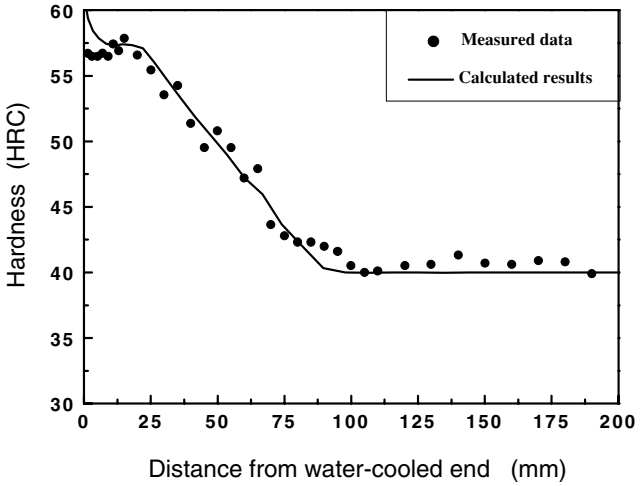

Fig. 9. Comparison between calculated and experimental hardness curves of AISI P20 steel.

estimated using empirical formulas (10) and shown in Fig. 9. As can been seen from the figure, except for the quenching end, the calculated results are in good agreement with the experimentally measured results.

Conclusion

1 A two-dimensional nonlinear finite element method was established to determine the temperature variation in a revised end-quenching test. The results show that the cooling rate is higher nearer to the quenching end, but becomes almost constant at the points beyond 110 mm away from the quenching end.

2 The calculated microstructure distribution indicates that martensite is formed in the region 0–25 mm from the quenching end and bainite exists in the region between 10–110 mm; and in the region beyond 110 mm from the quenching end, pearlite and a little fraction of ferrite are the fundamental constituents. The metallographic analysis fits the calculated results well.

3 The hardness predictions based on the empirical formulas are in agreement with the measured hardness profile.

References

1. Jominy WE, Boegehold AL. Trans ASM 1938: 26: 574–585.
2. Herring DH. Indust Heating 2001: 10: 81–86.
3. Marrow J. Indust Heating 2001: 9: 57–60.
4. Buchmayr B, Kirkaldy JS. J Heat Treating 1990: 8: 127–136.
5. Geary EA, Cook WT, Lane KAG. Mater Sci Forum 1994: 163–165: 689–696.
6. Li MV, Niebuhr DV, Meekisho LL, Atteridge DG. Metall Mater Trans B 1998: 29B: 661–672.
7. Andersson K, Kivivuori S, Korhonen AS. Mater Sci Forum 1994: 163–165: 683–688.
8. Post CB, Fetzen MC, Fenstermacher WH. Trans of ASM 1945: 35: 85–111.
9. Jatczak CF. Trans of ASM 1965: 58: 195–209.
10. Philippe LM, Tahar L, Eugene A, et al. Int J Therm Sci 2002: 41: 517–527.
11. Hömberg D. Acta Mater 1996: 44: 4375–4385.
12. Denis S, S Sjöström, A Simon. Metall Trans A 1987: 18A: 1203–1212.
13. Pan J, Li Y, Li D. J Mater Proc Technol 2002: 122: 241–248.
14. Tian D. Computational and experimental investigation of quenching process with abrupt changing boundary conditions. Ph.D Thesis, Shanghai Jiao Tong University, 1998.
15. Maynier P, Dollet J, Bastien P. Hardenability concepts with applications to steels, AIME, New York, NY 1978: 518.

Address:
Dr. Yao Xin
560, College of Materials Science & Engineering
Shanghai Jiao Tong University
1954 Huashan Road
Shanghai, 200030
China
e-mail: xin_yao@yahoo.com